Brief communication: Glacier run-off estimation using altimetry derived basin volume change: case study at Humboldt Glacier, Northwest Greenland.

Laurence Gray[1]

5 [1]Department of Geography, Environment and Geomatics, University of Ottawa, Ottawa, K1N 6N5, Canada

Correspondence to: Laurence Gray (laurence.gray@uottawa.ca)

Abstract. CryoSat can provide temporal height change around the Greenland Ice Sheet including that close to the terminus of many glaciers. Height change from the northern outlet of the Humboldt Glacier in north-western Greenland is combined with ice flux into and out of sections of the glacier basin to derive the water run-off each year from 2011 to 2019. The cumulative
10 nine-year run-off for this part of the Humboldt basin is 9.6 ± 2.9 km^3 and is predominantly subglacial at the terminus with large run-offs occurring in 2012, 2015 and 2019, and much smaller ones in 2013, 2016, 2017 and 2018.

1 Introduction

The recent 21st century increase in mass loss from the Greenland Ice Sheet (Mouginot et al., 2019, The IMBIE team, 2020, Smith et al., 2020) has emphasized the need for regular monitoring of the periphery of the ice sheet, the area which has been,
15 and still is, changing the most rapidly. While glacial ice discharge measurements are now widely available for Greenland outlet glaciers (e.g. King et al., 2018, and Mankoff et al., 2019), direct measurements of the surface and subglacial run-off are not. Water run-off represents an important contribution to the overall mass balance and is normally estimated using a regional climate model, e.g. the MAR model (Fettweis, et al., 2017, 2020).

The interferometric (SARIn) mode on the European Space Agency (ESA) CryoSat satellite (Parrinello et al., 2018) was
20 developed in part to alleviate the problems associated with measuring glacial ice height when surface slopes are relatively large, e.g., at the periphery of the Greenland Ice Sheet. Greenland outlet glacier termini are almost always in a local topographic low such that the 'point-of-closest-approach' (POCA) for a satellite pass across a glacier terminus is often displaced to adjacent higher elevation terrain. This effect coupled with the larger slopes and rough surfaces means that it is difficult to measure the height or height change of glacier termini reliably with the traditional radar altimetry technique; i.e. the estimation of the time-
25 of-arrival of the first radar returns. This suggests that 'swath mode' results (Gray et al., 2013), which use the part of the waveform beyond the POCA, may be useful for the height change in these regions, indeed that approach has been used here for the lower elevations of the northern branch of the Humboldt Glacier.

2 Data and Methods

2.1 Height change estimation using CryoSat

30   CryoSat baseline-C and -D intermediate level SARIn (L1b) data collected from the summer of 2010 to the end of 2019 have been used in this work. These are available from ESA and have been processed to terrain height and height change using the methods described in Gray et al., 2015, 2019. For the lower reaches of the tide-water glaciers I rely primarily on swath mode processing (Gray et al., 2013, Gourmelen et al., 2019). With swath mode processing it is important to select conditions which will minimize the contribution from any unwanted range ambiguous region. A good example of this effect was observed when

35   the height and height change of the surface of supra-glacial lakes were mapped using CryoSat swath mode data (Gray et al., 2017). The relatively flat lake provided a strong reflecting surface so that even though other ice terrain was range-ambiguous, their returns were small enough in relation to that from the lake that the differential phase reflected the cross-track look angle to the supra-glacial lake and allowed accurate geocoding and height estimation. In summer there is a strong probability of wet ice conditions close to the termini of tidewater glaciers, and this can lead to strong specular reflections. By using relatively

40   strong waveform returns (> -150 dB) from summer passes there is a good likelihood that the wet glacier surface will dominate the composite return signal and the differential phase will then more accurately reflect the cross-track look angle and allow accurate geo-coding.

There is a trade-off between the size of the patch over which the SARIn data is binned and the ability to extract temporal variation in height change. The shortest practical temporal sampling possible with CryoSat is the 30-day sub-cycle but then a

45   relatively large area is preferred to get adequate averaging (Gray et al., 2019). That approach is not appropriate for the relatively small areas close to the terminus of the Humboldt Glacier so the size of the temporal window can be increased to obtain more samples for averaging. Here the swath mode height data are sorted into overlapping spatial windows of size 2.4 km by 2.4 km sampled at 1.2 km spacing, and a search is done for closely spaced height estimates (< 100 m apart) in a succession of time periods. For the year-to-year height change, data from July 1 to October 15 were used to capture the possibility of strong

50   returns and to minimize the possibility of a varying bias between the surface and the CryoSat detected height (Gray et al., 2019). While the surface height at any point on the glacier will likely change during this period the relatively large temporal bin is not as big a problem as it might appear. The CryoSat satellite orbit repeats every 369 days so that when comparing the data from one year to the next many of the pairs will be close to one year apart in time and the average of the height change of all the possible pairs within the separation criteria will reflect the yearly height change even when using a temporal window

55   of three and a half months each year. The unit of time for the year-to-year work is then early fall in one year to the same period in the next.

While swath mode processing has provided results close to the glacier terminus in the region in which the POCA algorithms struggle, at higher elevations the surfaces are smoother, the slopes more moderate and POCA results tend to have lower random errors and a lower probability of bias errors (Gray et al., 2017). For this reason, POCA results were used at elevations above

60   ~600 m. The method used is similar to the swath processing approach outlined above although now the spatial bin size is

doubled to 4.8 km, the sampling is 2.4 km, and the search for pairs of points in the different time bins is carried out for separations less than 400 m. The GIMP DEM (Howat et al., 2014) is used for slope correction (Gray et al., 2019).

2.2 Mass change estimation using CryoSat

Satellite altimetry can provide volume change data directly, but not mass change. Often models are used to estimate the near surface density change and surface lowering in the accumulation zone associated with different summer conditions (Reeh et al., 2005), this can then allow the estimation of mass change. However, any model will depend on good weather data which is in limited supply around Greenland, and this applies to the Humboldt Glacier basin. Here I use the CryoSat data itself to estimate the surface lowering in the summer months in those areas in the percolation zone where there is no evidence of direct run-off through surface streams or moulins, and no evidence of a change in ice flux which could explain the height loss. Using the MAR model for 2010 to 2019, the elevation of the transition between net ablation and net accumulation varies in this area from ~ 1000 m to ~ 1300 m. Consequently, it is necessary to consider the effect of firn densification only at the higher elevations in our study area. To search for height change associated with firn densification it is necessary to use the 30-day temporal sampling and a relatively large area in the accumulation zone, $> \sim 10^3$ km^2. This is not an issue as conditions in the percolation zone change relatively slowly with position. Further, there are now 50 m resolution SAR data sets (Joughin, 2019) with repeat coverage every 6 days which show the initiation, extent and termination of the summer melt. Also, this imagery (see accompanying material) shows the positions of supra-glacial lakes and surface run-off streams. Consequently, when there is no evidence of extensive surface run-off to a lower elevation or change in surface ice speed it is possible to associate a relatively fast summer height loss over a large area in the accumulation zone with firn densification. This provides a straightforward method of correcting the volume loss to obtain an estimate of mass loss.

In the ablation zone the volume loss can be converted directly to a mass loss using the density of ice, here I use a density of 910 kg/m^3.

2.3 Ice velocity and gate flux estimation

Ice velocity data were obtained primarily from the NSIDC MEaSUREs (NASA's Making Earth System data records for Use in Research Environments) web site. Data from both radar (NSIDC-0481, -0478 and -0731, Joughin et al., 2018, 2020) and optical satellites (NSIDC-0646, Howat, 2017) have been used. For 2019, ice velocity data sets from the Programme for Monitoring of the Greenland Ice Sheet (PROMICE) have also been used (Solgaard and Kusk, 2019). Although the relative accuracy of the velocities derived from the optical satellites is lower than that from speckle tracking with SAR data, they are necessary to capture the speed changes in the summer melt season. The 'InSAR Selected Glacier Site Velocity Maps' produced from image pairs from the German Aerospace Centre's (DLR) twin satellites TerraSAR-X / TanDEM-X (TSX, Joughin et al., 2020) tend to have the lowest error estimates. Plots of the TSX speed variation across the terminus gate (gate 1 in Fig. 1) show that the shape of the velocity profile does not change with year or season although the magnitude does. For this reason, a reference point was selected and the speed across the gate from all the various sources was based on the reference TSX velocity

profile times the ratio of the velocities at the reference point. The temporal frequency of velocity estimates increases after 2014 and the spike in summer surface velocity can be tracked quite well. However, prior to 2014 we know there was a spike in the

95   summer gate velocity, but the timing and duration were not available from satellite imagery. GPS receivers had been used to track the seasonal change in surface speeds of eight Greenland outlet glaciers (Ahlstrøm et al., 2013), including one close to the terminus of the Humboldt Glacier. Unfortunately, this receiver was lost at the beginning of July 2012, but the onset and peak of the velocity spike were captured (Fig 9, Ahlstrøm et al., 2013). With this as a guide some extra velocity points were added for the summers of 2011 and 2012 to limit the temporal duration of the velocity peak measured by the optical satellites.

100   The temporal velocity data at the reference point were up sampled using linear interpolation to give daily speed estimates. Gate 1 (Fig. 1) is ~10.2 km wide with an average ice thickness of 360 m in 2011 decreasing to 321 m in 2019. The net ice flux through gate 1 is calculated by summing 75 flux estimates each using the average speed and ice thickness over a segment of width 137 m. The average ice thickness for gates 2, 3, and 4 is ~ 926, 1157 and 1422 m, the average speed is ~ 94, 56 and 35 m/year, and the cross-gate flux calculations are performed for segments of width 170, 187 and 2000 m. The relatively wide

105   segment for gate 4 was possible because of the nearly linear velocity variation across the gate. The flow lines were derived from the x- and y- components of the 200 m 2017-2018 velocity mosaic of Greenland (Joughin et al., 2015). The upstream end of the test area (gate 4 in Fig. 1) is orthogonal to the flow direction and the flow lines are derived from points on this gate separated by 2 km. When calculating the flux, the surface speed is normally used as the depth averaged speed whenever the surface speed is ~ 100 m/year or larger (Mankoff et al., 2018). To account for the possibility that the depth averaged speed for

110   gates 3 and 4 is less than the surface speed, fractions of the surface speed have been used; 0.95, .975, and 1 for gate 3, and 0.9, .95 and 1 for gate 4. Results are plotted for fractions of .975 (gate 3) and .95 (gate 4), the other values are used to estimate the potential error arising from the uncertainty in the depth averaged velocity.

'Bedmachine' data (Morlighem et al., 2017) were used primarily for the ice thickness data. However, the estimated ice thickness uncertainty was quite large for part of the terminus gate and interpolated IceBridge data were used instead. The 20

115   April 2013 IceBridge flight provided 10 lines separated by ~ 2 km in the flow direction over the northern Humboldt Glacier terminus and this allowed revised ice thickness using the MCoRDS data (Paden et al., 2019). The cross-sectional area of the other gates and associated errors were based on the Bedmachine data. Finally, the daily ice flux through the various gates can be summed to give nine yearly values from the fall of 2010 to the fall of 2019.

2.4 Water run-off estimation

120   The water run-off is estimated based on mass conservation. Surface height change data can be used to estimate the volume and mass change for that part of an outlet glacier basin defined by input and output crossflow gates connected by ice flow lines. The input expressed as mass per unit time is the sum of the ice, firn and water flux at an up-stream gate plus the contribution from surface precipitation, i.e., $M_{in} = \rho_i F_{ice\_in} + F_{water\_in} + \rho_f F_{firn\_in} + A. acc$, where F_{ice_in}, F_{firn_in} and F_{water_in} are the input fluxes of glacial ice, firn and water respectively. A is the surface area, acc is the accumulation in water equivalent per

125   unit area, ρ_i and ρ_f are the average densities of the ice and firn components and the unit of time is Sept. 1 in one year to Aug.

30 in the next. The yearly ice flux at a down-stream gate close to the glacier terminus can be estimated assuming that the gate cross-section is occupied by glacial ice and the possible fraction of air, snow or water in the gate cross-section is small enough in relation to the potential error in the gate cross-section that they can be ignored.

The mass change, or mass balance for a specific area, can be equated to the difference of input and output masses, $\delta M = M_{in} - M_{out}$, where δM is estimated based on changing surface heights derived from the CryoSat data. Here the area of the large basin extends up into the percolation zone so that while the height being measured is essentially the glacier surface, the density of the upper layers may change depending on the history of surface melt. The appropriate correction to the mass balance is based on the analysis of the CryoSat data, as outlined above in section 2.1, and described in more detail in the results for the northern arm of the Humboldt Glacier below. The total output at the terminus gate is $M_{out} = \rho F_{ice\_out} + F_{water\_out}$ so the excess water run-off for the defined part of the glacier basin can be calculated as

$$F_{water\ out} - F_{water\ in} = \rho(F_{ice\ in} - F_{ice\ out}) + A.\,acc - \delta M \qquad (1)$$

If the ice is much thicker at the upstream gates, as is the case with the Humboldt Glacier, the contribution of firn to the input flux is relatively small and much smaller than the potential error introduced by the uncertainties in ice thickness and the depth averaged velocity. The mass loss from evaporation and sublimation are also neglected as they are relatively small and again much less than the errors in the estimates of mass change and the difference in flux estimates.

2.5 Accumulation estimation

The MARv3.11 regional climate model of Greenland (Fettweis, 2020) has been used to provide the estimates of the yearly accumulation over the studied area of the Humboldt basin. These data are provided daily, sampled at 20 km and are available as mm. water equivalent per square meter. Here the data are up sampled to the Bedmachine grid (provided in polar stereographic coordinates at 150 m, Morlighem et al., 2017) using the Matlab function ScatteredInterpolant. Yearly accumulation data from September 1 to August 30 are summed for the three 'sub-basins' (Fig. 1) beginning with the 2010-2011 year and ending with 2018-2019.

3 Results

3.1 Run-off for the northern arm of the Humboldt Glacier

The calving front of the northern arm of the Humboldt Glacier has receded since 1975 (Carr et al., 2015) and, in common with many of the outlet glaciers on the west and north coasts of Greenland, the speed close to the terminus has also increased since ~ 2000 (Joughin et al., 2017, Hill et al., 2018). Figure 1 shows the position of the study area in the Humboldt Glacier basin and in Greenland. The four gates and the outer flow lines define 3 basins, the largest basin, no. 3, is contained within the outer flow lines and gates 1 and 4, while gates 2 and 3 define the upstream ends of the smaller basins, 1 and 2 respectively. The nine-year height loss, fall 2010 to fall 2019, is illustrated as a colour overlay on a SAR image (Sentinel 1 from 27 July 2019).

Note that the colour bar is non-linear and the bulk of the height loss, up to ~ 45m, is close to the terminus. During this period, the net mass loss from basin 3 was 11.3 ± 0.6 Gt but more than 50% of this was lost within 20 km of the glacier terminus.

The velocity data plotted in Fig. 2A show the speed at the reference point in gate 1 (Fig. 1), and the quite dramatic increase in summer velocity occurring after the onset of the melt period. From a sequence of 2019 Sentinel images in this area (see

160 supporting material) the onset of melt in 2019 began after June 6 but before June 13. The image from June 13 shows indications of wet snow up to an elevation of ~ 1300m. The first significant speed increase is plotted here with a nominal date of Jun 17 but this was derived from passes on June 5 and June 29 so we cannot be certain when in this period the relatively sudden jump in speed occurred. However, from Fig. 9, Ahlstrøm et al., 2013, we know that the 2012 speed increase happened over a few days at the beginning of July. Although there is less velocity data available for the upstream gates 2, 3 and 4 both the seasonal

165 and year-to-year variations are much less than that exhibited at the gate close to the terminus.

In calculating the ice fluxes through the four gates the reduction in ice thickness over the nine years was accounted for although the larger ice thickness and much smaller thinning rates at gates 3 and 4 lead to a small year-to-year correction. The cumulative ice flux at the terminus gate 1 is actually less than that estimated through the other three gates (Fig. 2B) up to ~2016, but due to the increase in average speed beginning after the 2014 summer, the cumulative ice flux across gate 1 exceeds that from any

170 of the other gates by the summer of 2018. The ice flux through gate 1 between fall 2018 and fall 2019 was 3.5 ± 0.2 km^3, more than twice the flux between fall 2010 and 2011. The ice volume loss in km^3 and the net mass balance in Gt for the three basins are shown in Figure 2C. All the years exhibit a negative mass balance except the fall 2012 to fall 2013 year which showed a small positive mass balance. Mass loss was largest for 2019 due to the unusual Greenland weather (Tedesco and Fettweis, 2020), and to the increased speed at the terminus.

175 Thirty-day height change data derived from all the CryoSat POCA data for basin 3 above 1300 m (Fig. 3) shows that there was a melt season height decrease in this area only in 2012, 2015 and 2019 (Fig. 3B). As there is no evidence of run-off to lower elevations or of an associated change in speed, I ascribe these height changes predominantly to surface melt and sub-surface refreezing, i.e., firn densification, and reduce the volume loss using these values so that the mass loss can be estimated. The average summer height losses associated with densification (Fig. 3B) were 0.42 ± 0.08 m (2012), 0.45 ± 0.08 m (2015) and 0.4

180 ± 0.08 m (2019) based on the 44,756 POCA height results spanning the nine years and the area of basin 3 above 1300 m.

The cumulative net run-off for the three basins (Fig. 2D) is estimated based on the ice flux difference between input and out, the accumulation and the net change in basin mass, as described in section 2.4 above. By the fall of 2019, the cumulative run-off for basin 2 is comparable to that for the larger basin 3. As the larger basin contains the smaller one, the run-off from the larger basin cannot be less than the smaller one, however, by examining the temporal imagery for 2019, the year with the

185 largest negative mass balance, there is no clear evidence of surface run-off to lower elevations above gate 3, although there is evidence for wet snow (see the supporting material). Consequently, this result is not as suspicious as at first sight, indeed it suggests that the majority of the run-off originates from below gate 3 in all years.

Figure 2E shows the run-off at gate 1 for each year from both basins 1 and 2. Basin 2 run-off peaked in 2012 and 2019 with values approaching 2 km^3, 2011 and 2015 also had relatively large values ~ 1.3 – 1.5 km^3, and the lowest run-offs (~ 0.4 – 0.6

190   km^3) occurred in 2013, 2016, 2017, and 2018. Although the uncertainty estimates in Fig. 2E are relatively large it is still gratifying to see that in the years with low run-offs the difference between the basin 1 and 2 run-offs also decreases. Indeed, the small difference implies that in the four years with low run-off it originated primarily from basin 1.

3.2 Errors

Errors can be introduced into the estimates for excess run-off through errors in the four terms in equation (1); the input and
195   output ice fluxes, the accumulation, and the mass change. These are derived from ice velocity, ice thickness, the integrated accumulation over the various basins, and the volume change derived from the CryoSat heights. If we assume that the errors in the four terms are independent, then the error in the run-off can be estimated as the square root of the sum of the squares of the error in the four individual terms. The MEaSUREs velocity, PROMICE velocity and Bedmachine data have associated error estimates and these data have been used to estimate the errors in the fluxes through the four gates. Normally, the error in
200   gate flux is dominated by the error in the ice thickness (Mankoff et al., 2019). However, for gates 3 and 4 the surface speeds are relatively low, ~57 m/year and ~35 m/year, and it is possible that the depth averaged velocity is a fraction of the surface velocity. By choosing a range for the possible fraction, 0.9, .95 and 1 for gate 4 and 0.95, .975 and 1 for gate 3, the possible impact of the fraction variation can be evaluated. The uncertainty in the depth averaged velocity for gates 3 and 4 then becomes the dominant source of error for the ice flux through these gates.

205   The potential error in the volume change term in the equation for run-off arises from errors in the CryoSat heights and the additional error in the height change due to the possibility of near surface densification of the firn layer in the percolation zone at the higher elevations in basin 3. For each of the spatial bins and temporal separations there are 9 estimates of the year-to-year height change, one direct and 8 indirect involving a third time period (Gray et al., 2019). For the '30-day' height change in the percolation zone (Fig. 3B) there were 117 height change estimates for each spatial and temporal bin, 1 direct and 116
210   indirect. For this data, the average standard error of the mean of the POCA and swath-mode heights were ~8 and ~20 cm, respectively. However, this gives an optimistic picture for the precision of the height measurement as it ignores the possibility of varying bias errors creeping into the results (Gray et al., 2019). Using summer-fall data should minimize the error due to a changing bias between the actual surface and the height derived by the processing algorithm (Gray et al., 2019). Nevertheless, an additional possible bias error of ±10 cm was added to the standard error in calculating the overall error in the yearly water
215   volume changes.

The ±20% error in the estimate of net accumulation over the 3 sub-basins is based on the comparison of accumulation made by the IceBridge snow radar and the MAR regional climate model (Koenig et al., 2016).

It is important to note the difference in the way that errors propagate for the different components of the equation for run-off. The mass change term is based on the altimetry derived volume change and the error in the comparing the volume between
220   any two years is approximately the same, i.e., the error in the volume or mass change between 2011 and 2012 is essentially the same as between 2011 and 2019. But this is not the case for the flux estimates where an error in e.g., the cross-sectional

area of an ice gate will accumulate such that the error in flux over nine years could be nine times the error over one year. This is the source of the increasing error estimates with time in Fig. 2D.

4 Discussion

4.1 Velocity change at the terminus over the nine years

Each year the velocity data show a spike in summer speed at the terminus gate associated with the melt water production. The sudden speed up, and the apparent lack of surface run-off channels near the terminus gate suggest that here the bulk of the run-off happens sub-glacially. The summer variation in surface velocity appears to fit the pattern of speed up associated with increasing basal water pressure in a distributed, inefficient subglacial drainage system followed by a transition to a more efficient drainage system as channels develop. With the improved drainage system, the sub-glacial water run-off increases but the surface speed decreases as the basal water pressure falls and basal drag increases (Flowers, 2016). As well as the yearly spike in surface speed near the terminus, there is a steady increase in speed after the 2013 melt period which continues through all the seasons until after the 2019 melt when the speed reverts to a value less than the value prior to the 2019 spike in velocity. The cause of the year-to-year speed increase at gate 1 after the 2013 summer speed spike may be related to a reduction in basal drag associated with the steady thinning in the terminus region, nominally around 4 - 5 m/year. The issue then is why there has been such a large loss of ice through both retreat and thinning at the glacier terminus in such a short time. As a tide-water glacier this involves ice-ocean interactions (Rignot et al., 2016, Flowers, 2018), ice-sea ice interactions (Joughin et al. 2020) and the detailed basal topography (Carr et al., 2015): these issues are beyond the scope of this paper.

4.2 Water run-off: source and timing

Measuring basin run-off in this way depends on the difference in ice flux at two gates, one upstream but connected by flow lines to the lower gate near the terminus. If the cross-section at either gate is occupied by water, and if that changes year-to-year then there is a possibility of a bias error in the run-off estimate. By picking the fall time period for the year-to-year volume and flux estimates it is reasonable to assume that any subglacial water flow that still exists is relatively efficient and that the fraction of the gate cross-section occupied by the water would be small. Certainly, the result that the estimated run-off peaked in years with large surface melts suggests an efficient subglacial hydrologic system year-to-year. Further, the short spike in speed each summer suggests a relatively rapid transition to the more efficient channelized subglacial outflow. Consequently, even if a fraction of the cross-section of gate 1 in the fall is not solid ice, the impact on this method should be small.

4.3 Applicability of this method

If there was a steady input of englacial or subglacial water at the upper gate and an equal amount of water leaving at the lower gate at the same time this would not be detected with this method. However, around Greenland there is both ice discharge and

water run-off, and as the run-off is predominantly seasonal it can be estimated with this method. However, the method will be more challenging for those areas and glaciers with strongly divergent upstream flowlines.

5 Conclusions

In this paper I show that the interferometric mode of the CryoSat radar altimeter can be used to measure the change in volume
255 of part of the basin of a relatively fast flowing Greenland glacier on a yearly basis. By combining this with ice flux measurements, yearly accumulation estimates and a correction for firn densification related to unusual melt into the accumulation zone, it is possible for the first time to derive useful estimates of the yearly water run-off directly from satellite data.

This approach also permits a direct comparison of water run-off and mass discharge as icebergs. Initially the run-off in this
260 basin was comparable to the ice discharge, however, after the increase in gate 1 speed in the fall of 2014 the ice discharge exceeded the run-off such that by the fall of 2019 the cumulative ice discharge over the nine years was about two times larger than the run-off. Not surprisingly, most of the run-off originated from the ablation zone. This reduces the potential errors in run-off which could arise from a bias in mass balance estimate due to problems with the surface densification in the percolation zone and also any bias error due to errors in the depth-averaged ice velocity at the upper gate.

265 There is a relatively large variation in run-off year-to-year, e.g., the run-off in 2012 was about four times larger than that in 2013, although the ice flux was comparable in the two years. This highlights the benefit of a methodology which provides results on a yearly basis and allows comparison with year-to-year conditions. This is preferable to the approach which averages the mass balance over many years or uses a model for the seasonal or year-to-year variation.

The new generation of satellite altimeters, CryoSat launched in 2010 and now IceSAT-2 launched in 2018, provide height and
270 height change data which allow mass balance estimation at better spatial and temporal resolutions than was possible prior to the CryoSat launch. The use of swath-mode processing for the low elevations at the terminus of the Humboldt Glacier helped provide the height change data necessary to capture the large height loss in this region.

Satellite radars and laser altimeters can track temporal height change associated with the sometimes-episodic movement of subglacial water. It is conceivable that over time the new altimeter systems and this approach could also be used to estimate
275 the source, movement and volume of subglacial water. In the current example it is clear that significant flux of water only begins downstream of gate 3 and that in these nine years more than 70% originated below gate 2. In low melt years virtually all the run-off originated from below gate 2.

Acknowledgements

This work was supported by the European Space Agency through the provision of CryoSat-2 and Copernicus Sentinel-1 SAR
280 data. The velocity data was provided primarily by the NASA MEaSUREs programme and available from the NSIDC web site.

NASA supported the IceBridge (OIB) flights over Greenland, while NSIDC facilitated provision of the BedMachine and airborne OIB data. Ice velocity data for 2019 were produced as part of the Programme for Monitoring of the Greenland Ice Sheet (PROMICE) using Copernicus Sentinel-1 SAR images distributed by ESA and were provided by the Geological Survey of Denmark and Greenland (GEUS) at http://www.promice.dk. Comments and help provided by Dave Burgess, GSC Canada,
285 on an earlier version of this communication are gratefully acknowledged.

Data Availability

The various MEaSUREs velocity data sets are available from NSIDC (https://nsidc.org/data/measures/data_summaries), the IceBridge ice thickness data at https://doi.org/10.5067/GDQ0CUCVTE2Q (Paden et al., 2010). CryoSat-2 data are available from the European Space Agency (https://science-pds.cryosat.esa.int/, last access: 31 April 2019; ESA, 2019). Bedmachine
290 data (Version 3) are available from https://nsidc.org/data/IDBMG4. The temporal sequence of 2019 Sentinel images are available from the supporting material. Other data and code are available from the author upon request.

Author Contribution

L. Gray completed all the work for this publication.

Competing Interests

295 There are no competing interests involved in publication of this work.

References

Ahlstrom, A. P., Andersen, S. B., Andersen1, M. L., Machguth1, H., Nick, F. M., Joughin, I., Reijmer, C. H. , van de Wal, R. S. W., Merryman Boncori, J. P., Box, J. E., Citterio1, M., van As, D., Fausto, R. S., and Hubbard A.: Seasonal velocities of eight major marine-terminating outlet glaciers of the Greenland ice sheet from continuous in situ GPS instruments. Earth Syst. Sci. Data, 5, 277–287, www.earth-syst-sci-data.net/5/277/2013/doi:10.5194/essd-5-277-2013, 2013.

Carr, J. R., Vieli, A., Stokes, C. R., Jamieson, S. S. R., Palmer, S. J., Christoffersen, P., Dowdeswell, J. A., Nick, F. M., Blankenship, D. D., and Young, D. A.: Basal topographic controls on rapid retreat of Humboldt Glacier, northern Greenland, J. Glaciol., 61, 137–150, https://doi.org/10.3189/2015JoG14J128, 2015.

Fettweis, X., Box, J. E., Agosta, C., Amory, C., Kittel, C., Lang, C., van As, D., Machguth, H., and Gallée, H.: Reconstructions of the 1900–2015 Greenland ice sheet surface mass balance using the regional climate MAR model, The Cryosphere, 11, 1015-1033, https://doi.org/10.5194/tc-11-1015-2017, 2017.

Fettweis, X.: MAR data, available at: ftp://ftp.climato.be/fettweis/MARv3.10/Greenland/NCEP1_1948-2019_20km/, last access: 30 March 2020.

Flowers, G. E.: Modelling water flow under glaciers and ice sheets, P. Roy. Soc. Lond. A, 471, 2176, https://doi.org/10.1098/rspa.2014.0907, 2015

Flowers, G.E. Hydrology and the future of the Greenland Ice Sheet. Nat Commun. 9, 2729. https://doi.org/10.1038/s41467-018-05002-0, 2018.

Gray, L., Burgess, D., Copland, L., Cullen, R., Galin, N., Hawley, R., and Helm, V.: Interferometric swath processing of CryoSat data for glacial ice topography, The Cryosphere, 7, 1857–1867, https://doi.org/10.5194/tc-7-1857-2013, 2013.

Gray, L., Burgess, D., Copland, L., Demuth, M. N., Dunse, T., Langley, K., and Schuler, T. V.: CryoSat-2 delivers monthly and inter-annual surface elevation change for Arctic ice caps, The Cryosphere, 9, 1895–1913, https://doi.org/10.5194/tc-9-1895-2015, 2015.

Gray, L., Burgess, D., Copland, L., Dunse, T., Langley, K., and Moholdt, G.: A revised calibration of the interferometric mode of the CryoSat-2 radar altimeter improves ice height and height change measurements in western Greenland, The Cryosphere, 11, 1041–1058, https://doi.org/10.5194/tc-11-1041-2017, 2017.

330

Gray L, Burgess D, Copland L, Langley K, Gogenini P, Paden J, Leuschen C, van As D, Fausto R, Joughin I and Smith B.: Measuring Height Change Around the Periphery of the Greenland Ice Sheet With Radar Altimetry. Front. Earth Sci. 7:146. doi: 10.3389/feart.2019.00146, 2019.

335   Hill, E. A., Carr, J. R., Stokes, C. R., and Gudmundsson, G. H.: Dynamic changes in outlet glaciers in northern Greenland from 1948 to 2015, The Cryosphere, 12, 3243–3263, https://doi.org/10.5194/tc-12-3243-2018, 2018.

Howat, I. 2017, updated 2019. MEaSUREs Greenland Ice Velocity: Selected Glacier Site Velocity Maps from Optical Images, Version 2.1. Boulder, Colorado USA. NASA National Snow and Ice Data Center Distributed Active Archive Center. doi:
340   https://doi.org/10.5067/VM5DZ20MYF5C. [Last accessed July 2020].

Howat, I., Negrete, A., and Smith, B.: The Greenland Ice Mapping Project (GIMP) land classification and surface elevation data sets, The Cryosphere. 8. 1509-1518. https://doi.org/10.5194/tc-8-1509-2014, 2014.

345   The IMBIE Team: Mass balance of the Greenland Ice Sheet from 1992 to 2018.: Nature 579, 233–239, https://doi.org/10.1038/s41586-019-1855-2, 2020.

Joughin, I., Smith, B. E., and Howat, I.: Greenland Ice Mapping Project: ice flow velocity variation at sub-monthly to decadal timescales, The Cryosphere, 12, 2211–2227, https://doi.org/10.5194/tc-12-2211-2018, 2018.

350

Joughin, I., Smith, B., Howat, I., and Scambos, T.: 2015, updated 2018. MEaSUREs Greenland Ice Sheet Velocity Map from InSAR Data, Version 2.1 Boulder, Colorado USA. NASA National Snow and Ice Data Center Distributed Active Archive Center. doi: https://doi.org/10.5067/OC7B04ZM9G6Q. [Accessed Jan. 2020].

355   Joughin, I., Howat, I., Smith, B. and Scambos, T.: 2020, MEaSUREs Greenland Ice Velocity: Selected Glacier Site Velocity Maps from InSAR, Version 2.0. Boulder, Colorado USA. NASA National Snow and Ice Data Center Distributed Active Archive Center. doi: https://doi.org/10.5067/JQHJUOYCF2TE. [Last accessed July 2020].

Joughin, I. 2017, updated 2019. MEaSUREs Greenland Image Mosaics from Sentinel-1A and -1B, Version 2.2. Boulder,
360   Colorado USA. NASA National Snow and Ice Data Center Distributed Active Archive Center. doi: https://doi.org/10.5067/GPVL3SACPBW4. [Last accessed July 2020].

Joughin, I. 2018, updated 2019. MEaSUREs Greenland Monthly Ice Sheet Velocity Mosaics from SAR and Landsat, Version 1. Boulder, Colorado USA. NASA National Snow and Ice Data Center Distributed Active Archive Center. doi:
365   https://doi.org/10.5067/OPFQ9QDEUFFY. [Last accessed July 2020].

Joughin, I., Shean, D. E., Smith, B. E., and Floricioiu, D.: A decade of variability on Jakobshavn Isbræ: ocean temperatures pace speed through influence on mélange rigidity , The Cryosphere, 14, 211–227, https://doi.org/10.5194/tc-14-211-2020, 2020.

370

King, M. D., Howat, I. M., Jeong, S., Noh, M. J., Wouters, B., Noël, B., and van den Broeke, M. R.: Seasonal to decadal variability in ice discharge from the Greenland Ice Sheet, The Cryosphere, 12, 3813–3825, https://doi.org/10.5194/tc-12-3813-2018, 2018.

375   Koenig, L. S., Ivanoff, A., Alexander, P. M., MacGregor, J. A., Fettweis, X., Panzer, B., Paden, J. D., Forster, R. R., Das, I., McConnell, J. R., Tedesco, M., Leuschen, C., and Gogineni, P.: Annual Greenland accumulation rates (2009–2012) from airborne snow radar, The Cryosphere, 10, 1739–1752, https://doi.org/10.5194/tc-10-1739-2016, 2016.

Morlighem, M., Williams, C. N., Rignot, E., An, L., Arndt, J. E., Bamber, J. L., Catania, G., Chauché, N., Dowdeswell, J. A.,
380   Dorschel, B., Fenty, I., Hogan, K., Howat, I., Hubbard, A., Jakobsson, M., Jordan, T. M., Kjeldsen, K. K., Millan, R., Mayer, L., Mouginot, J., Noël, B. P. Y., O'Cofaigh, C., Palmer, S., Rysgaard, S., Seroussi, H., Siegert, M. J., Slabon, P., Straneo, F., van den Broeke, M. R., Weinrebe, W., Wood, M., and Zinglersen, K. B.: BedMachine v3: Complete Bed Topography and Ocean Bathymetry Mapping of Greenland From Multibeam Echo Sounding Combined With Mass Conservation, Geophys. Res. Lett., 44, 11051–11061, https://doi.org/10.1002/2017GL074954, 2017.

385

Morlighem, M. et al. 2017, updated 2018. IceBridge BedMachine Greenland, Version 3. Boulder, Colorado USA. NASA National Snow and Ice Data Center Distributed Active Archive Center. doi: https://doi.org/10.5067/2CIX82HUV88Y. [Accessed May 2020].

390   Paden, J., Li, J., Leuschen, C., Rodriguez-Morales, F. and Hale. R.: 2010, updated 2019. IceBridge MCoRDS L2 Ice Thickness, Version 1.2. Boulder, Colorado USA. NASA National Snow and Ice Data Center Distributed Active Archive Center. doi: https://doi.org/10.5067/GDQ0CUCVTE2Q. [Last accessed July 2020].

Parrinello, T., Shepherd A., Bouffard J., Badessi S., Casal T., Davidson M., Fornari M., Maestroni E., and Scagliola M.:
395   CryoSat: ESA's ice mission – Eight years in space. Adv. Space Res., https://doi.org/10.1016/j.asr.2018.04.014, 2018.

Reeh, N., Fisher, D. A., Koerner, R. M., and Clausen, H. B. (2005). An empirical firn-densification model comprising ice lenses. Ann. Glaciol. 42, 101–106. doi:10.3189/172756405781812871, 2005.

400   Rignot, E., Xu, Y., Menemenlis, D., Mouginot, J., Scheuchl, B., Li, X., Morlighem, M., Seroussi, H., van den Broeke, M., Fenty, I., Cai, C., An, L., and de Fleurian B.: Modeling of ocean-induced ice melt rates of five west Greenland glaciers over the past two decades, Geophys. Res. Lett., 43, 6374–6382, doi:10.1002/2016GL068784. https://doi.org/10.1002/2016GL068784, 2016.

405   Smith, B., Fricker, H.A., Gardner, A.S., Medley, B., Nilsson, J., Paolo, F.S., Holschuh, N., Adusumilli, S., Brunt, K., Csatho, B., Harbeck, K., Markus, T., Neumann, T., Siegfried, M.R. and Zwally, J..: Pervasive ice sheet mass loss reflects competing ocean and atmosphere processes. Science, 12 Jun 2020: Vol. 368, Issue 6496, pp. 1239-1242, doi:10.1126/science.aaz5845, 2020.

410   Solgaard, A., and Kusk, A. (2019). Programme for monitoring of the Greenland ice sheet (PROMICE): Greenland ice velocity. Geological survey of Denmark and Greenland (GEUS). https://doi.org/10.22008/promice/data/sentinel1icevelocity/greenlandicesheet/v1.0.0 [Last accessed July 2020].

Tedesco, M. and Fettweis, X.: Unprecedented atmospheric conditions (1948–2019) drive the 2019 exceptional melting season
415   over the Greenland ice sheet. The Cryosphere, 14, 1209–1223, 2020, https://doi.org/10.5194/tc-14-1209-2020.
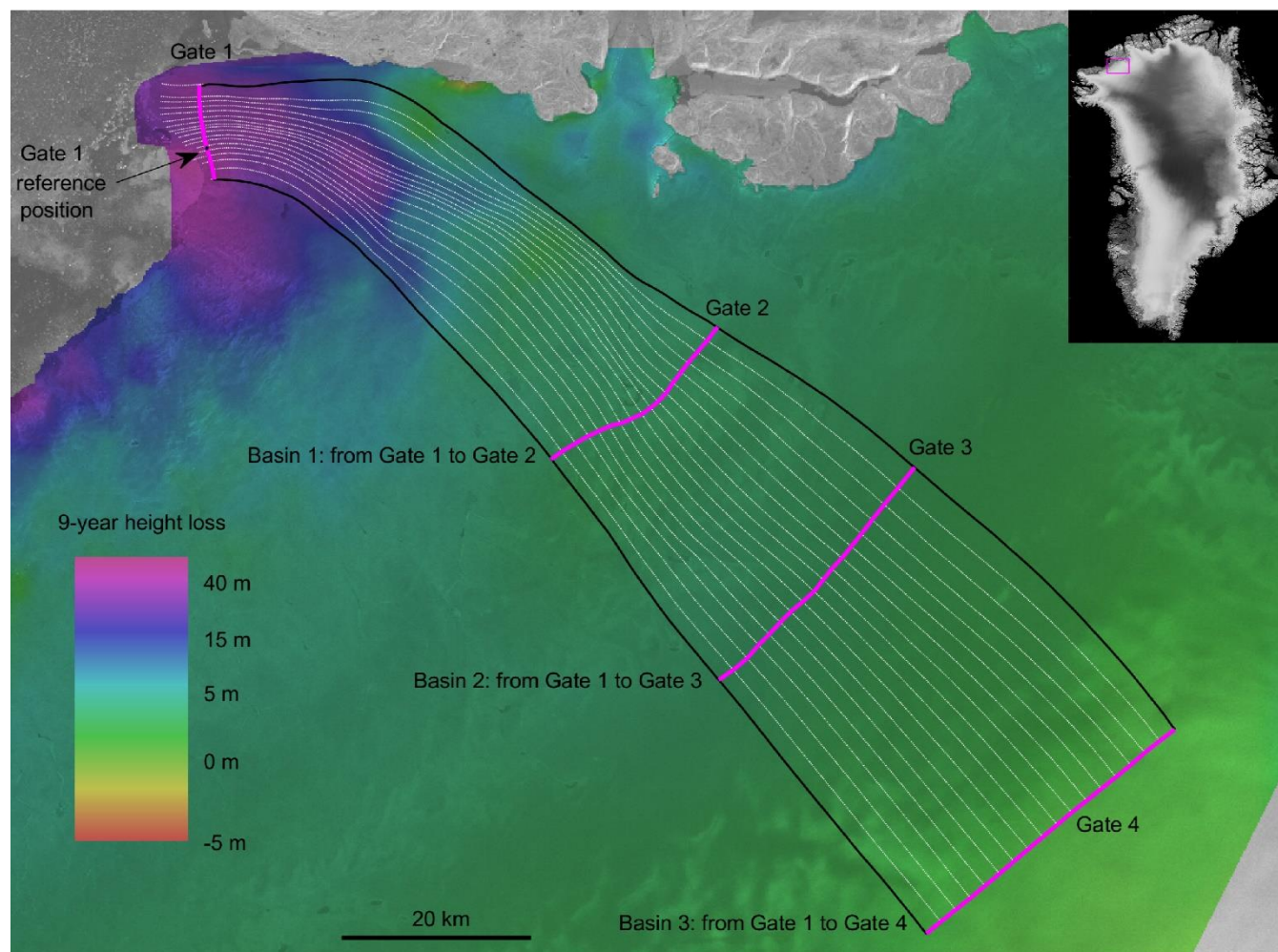
Figure 1: The positions of the 3 basins are defined by the 4 gates and the outer black flow lines. The white lines are also flow lines derived from the x- and y-components of the 2018-2019 200m MEaSUREs velocity product. The 9-year height loss is illustrated by the colour overlay on the Sentinel SAR image from 27 July 2019. This image is also used to show the position of the test area in the insert image of Greenland.
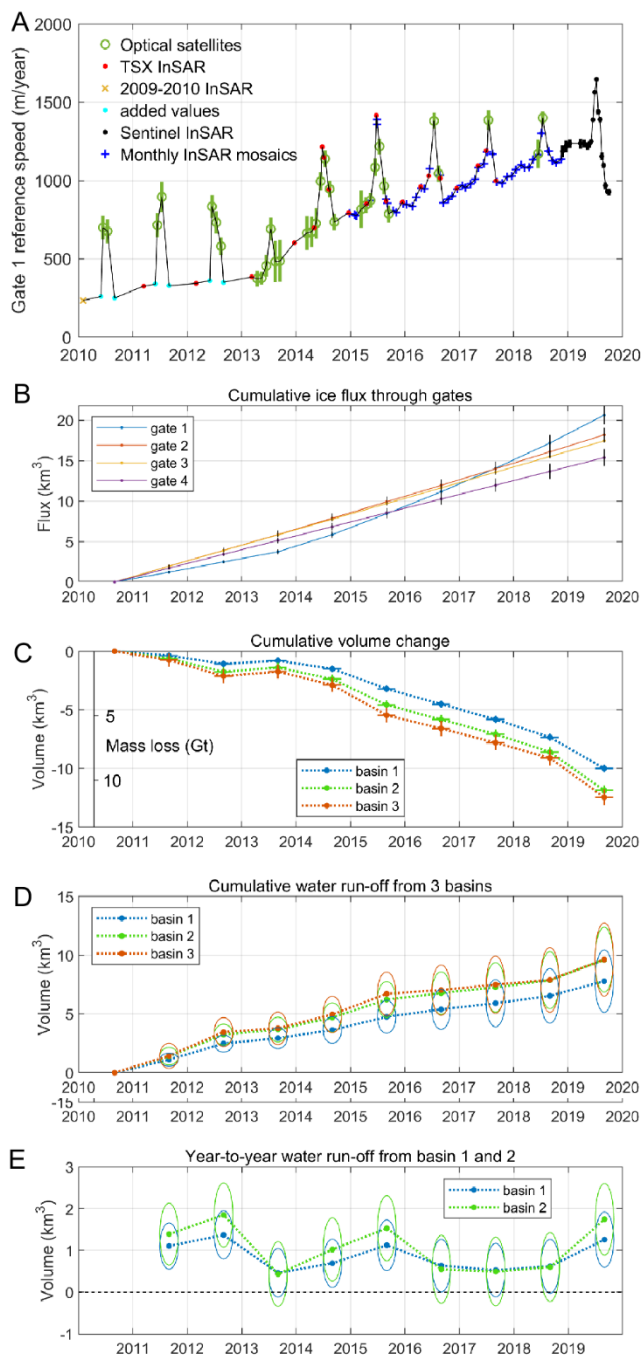
Figure 2: A: Temporal variation in surface speed at the reference point on gate 1. B: Cumulative ice flux through the 4 gates. C: Cumulative volume of ice and mass lost by the three basins over the nine years. D: Cumulative water run-off from the three basins. The ellipses around each point are an indication of (vertically) the potentially uncertainty in the result and (horizontally) the time period of the CryoSat data used in estimating the volume change. E: Year-to-year variation in water run-off from basins 1 and 2.

430
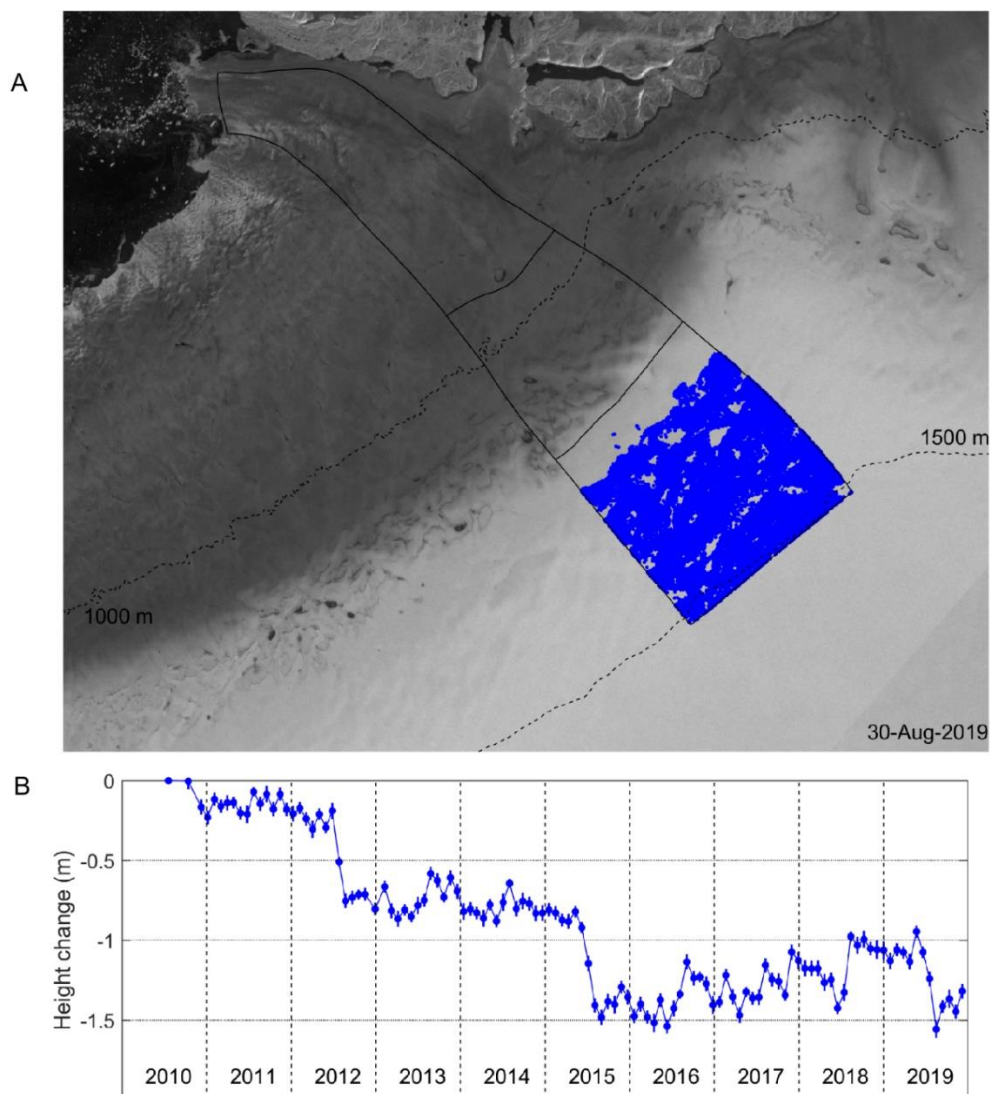
Figure 3. A: Part of the 30-Aug. 2019 Sentinel SAR image showing the positions (blue dots) of the 44,756 CryoSat POCA height
435 **estimates which were used in deriving the average 30-day temporal height change plot shown in B. The short vertical lines at each**
point are ±2 times the standard error of the mean of the 117 height change estimates for each point and are an indication of the
random error in the results.